Scanning error detection and compensation algorithm for white-light interferometry

Kaihua Cui, Qian Liu*, Xiaojin Huang, Hui Zhang, Lulu Li

Institute of Machinery Manufacturing Technology, China Academy of Engineering Physics, 64th Mianshan Road, Mianyang, Sichuan 621000, China

ARTICLE INFO

ABSTRACT

As the primary error source in white-light interferometry (WLI), the error of scanning steps directly affects coherence peak sensing and greatly lowers the measurement accuracy. Based on the least-squares iterative algorithm, we present an algorithm to detect and compensate for scanning error in WLI. The actual scanning step is calculated from the continuous moving fringes with an iterative algorithm, and the surface is reconstructed with the calculated scanning steps to make compensation. Both simulations and experiments indicate that the high-accuracy measurements can be implemented under disturbance over a wide frequency band. The proposed algorithm could relax the environment requirement of white-light interferometer application.

1. Introduction

White-light interferometry (WLI) is a fast and non-contact method for surface topography measurement, and is regarded as the standard tool [1–3]. WLI resolves phase ambiguity by using low-coherence light, and is not limited by $\lambda/4$ ambiguity that occurs in the single-wavelength interferometry [4]. Therefore, WLI is particularly suitable for rough surfaces and discontinuous structures measurements [5]. To determine the zero fringe order, WLI scans the object vertically and analyses the peaks of coherence envelopes in pixel-wise. WLI signal presents the maximum modulation value when the optical path difference between the test and reference light beams is zero. By locating the vertical position of envelope peaks, the surface height can be reconstructed. Furthermore, to achieve more accurate measurement, white-light phase-shifting interferometry (WLPSI), combining phase-shifting interferometry (PSI) and WLI, calculates the phase value of the point closest to the envelope peak and makes height correction [6,7]. Thus, WLPSI reaches the same vertical resolution as PSI on the sub-nanometer level, and expands its application in the measurement of optics.

For both WLI and WLPSI, coherence peak sensing is ensured by accurate vertical scanning. However, due to the scanner defects or environmental vibration, actual scanning steps deviate from the preset value, and scanning error is caused. Scanning errors can be directly drawn into envelope peak localization and phase calculation, lowering the measurement accuracy. Hence, WLI and WLPSI are not suitable for being used in the environmental disturbance. A variety of vibration compensation methods have been developed, and can be divided into two sorts. One sort is active compensation methods, in which a closed-loop feedback system is designed to monitor and compensate for scanning steps in real time. In these methods, a reference signal formed by high-coherence light [8] or acousto-optic tunable filter [9] is used to monitor vibration and provide feedback information for the scanner. Active compensation methods are performed during measurement, which are effective but suffer from their complicated configuration, large volume, and high cost. The other sort is passive compensation methods, which compensate for scanning errors by algorithms after measurement. Tereschenko et al. [10] measure the actual scanning position by a built-in distance measuring interferometer and reconstruct the correct WLI signals with least-squares method. This method depends on the accuracy of distance measurement, and the configuration is still complicated. Schmit et al. [11] assume the scanning steps remain constant among adjacent six frames and calculate steps with the phase-shifting algorithm. Schmit's method could compensate for the low-frequency scanning errors effectively, and has good compatibility with different types of interferometers. However, the assumption of local constancy of steps allows this method to compensate only for low-frequency errors.

In this paper, we present a novel detection and compensation algorithm for scanning error over a wide frequency band in WLI and WLPSI. The algorithm calculates scanning steps with an iterative algorithm from white-light interferograms without assumptions. Then the modulation and phase are calculated with least-squares method, and the surface topography is reconstructed accurately. We first describe the principle of the proposed algorithm, then verify it with simulations and experiments, and finally discuss the limitation of step error calculation and the impact of harmonic vibration.

---

* Corresponding author.
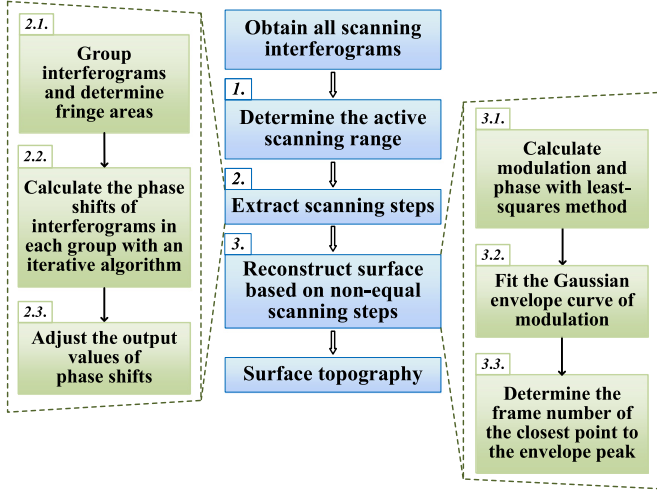 *E-mail address:* liuqianblue@126.com (Q. Liu).

Fig. 1. Flowchart of the proposed algorithm.

2. Method descriptions

In WLI, the intensity of a point on the measured surface along the vertical scanning interferograms can be expressed as

$$I_m = a + b \exp\left[-\left(\frac{2\pi(z_m - h)}{l_c}\right)^2\right] \cos\left[\frac{4\pi}{\lambda_0}(z_m - h) + \varphi_0\right], m = 1, 2, \cdots \tag{1}$$

where a is the background intensity, and $b = \gamma a$, where γ is the fringe contrast. λ_0 and l_c are respectively the equivalent wavelength and the coherence length of the Gaussian spectrum light source. z_m is the mth scanning position along the vertical axis, and h represents the surface height. The phase offset between the test and reference light beams, φ_0, depends on the surface materials. In Eq. (1), the pixel coordinate x of I_m, a, γ, b, and h is omitted. Here, x is a 2D symbol.

In the ideal case, scanner moves at a constant velocity, and the vertical scanning position z_m in Eq. (1) varies by a constant value, i.e. the step value. However, under the environmental vibration, steps are disturbed and become non-equal and unknown. Therefore, the key to accommodating WLI to the vibration environment is extracting steps accurately from the vibration-disturbed interferograms. Taking advantage of the continuous movement of fringes, the proposed algorithm calculates steps by analysing fringe movements. The flowchart of the proposed algorithm is shown in Fig. 1.

Step 1: Determine the active scanning range

To ensure the integrity of the measured surface during scanning, the focus range of the objective lens needs to cover from the top to the bottom of the surface in the imaging area. The interferograms outside of the focus range do not contain interference fringes and should be eliminated. The active scanning range can be determined by using sharpness evaluation. In this study, the Sobel operator is used to evaluate the sharpness of each interferogram. If the sharpness of an interferogram is less than a threshold, the interferogram is eliminated. The interferograms having significant sharpness are regarded as in the active scanning range.

Step 2: Extract scanning steps

Because the envelope peak position and phase calculations highly depend on the accuracy of scanning step extraction, it is crucial to calculate the actual values of scanning steps. In this study, a least-squares iteration is employed to calculate steps. The detail of scanning step extraction is as follows.

Step 2.1: Group interferograms and determine fringe areas

The interferograms in the active scanning range are divided into groups that contain adjacent N frames each. And adjacent groups have an overlap of at least one frame to ensure the continuity of calculated steps in the whole active scanning range. For each group, it can be considered that the background and modulation in Eq. (1) are approximately constant from frame to frame. The fringe intensity of the jth frame in the ith group can be written as

$$I_{j|i}(x) = A_i(x) + r_{j|i} B_i(x) \cos\left[\varphi_i(x) + \delta_{j|i}\right], x \in D_i, j = 1, 2, \cdots, N, \tag{2}$$

where x is the 2D pixel coordinate and $j|i$ represents the jth frame in the ith group; A, B, and φ are the background, modulation amplitude, and phase distribution; r and δ are the modulation variation factor and vibration-disturbed phase shift amount. Compared with Eq. (1), $A_i(x)$ corresponds to $a(x)$, and the exponential component is approximated as 1 so that $B_i(x)$ corresponds to $b(x)$; $\delta_{j|i} = 4\pi(z_{j|i}-z_{1|i})/\lambda_0$, and $\varphi_i(x) = 4\pi[z_{1|i}-h(x)]/\lambda_0+\varphi_0$. In each group, the fringe area D is determined by evaluating the pixel grayscale variation. If the grayscale variation (e.g., the standard deviation) of a pixel is larger than a threshold, the pixel is regarded as a pixel in the fringe area D.

Step 2.2: Calculate the phase shifts of interferograms in each group with an iterative algorithm

The iterative algorithm has been widely used in PSI to calculate phase shift and wavefront. After proposed by Okada et al. [12], an advanced iterative algorithm was developed by Wang et al. [13]. Furthermore, Liu et al. extract phase shift and wavefront from interferograms with background and contrast fluctuations [14,15]. Based on the single-wavelength interferometric model, iterative algorithms calculate wavefront phase and phase shift amount accurately by solving a large equation set. The actual phase shift amount can be either equal or random. However, WLI has a different model from single-wavelength interferometry, and high-contrast fringes in white-light interferograms only appear in a small area. It is impossible to apply the least-squares iterative algorithm (LSQ-IA) directly to all pixels to calculate the phase shifts. Hence, we applied the algorithm in Ref. [14,15] to the pixels in the fringe area D. Each iteration cycle contains two steps that are described as follows:

First, the parameters $r_{j|i}$ and $\delta_{j|i}$ are assumed as knowns to calculate the phase distribution $\varphi_i(x)$. For each pixel x in the fringe area, the phase is

$$\varphi_i = \arctan\left(-\frac{q_i}{p_i}\right), \tag{3a}$$

where

$$\begin{bmatrix} A_i \\ p_i \\ q_i \end{bmatrix} = \begin{bmatrix} N & \sum_j r_{j|i} c_{j|i} & \sum_j r_{j|i} s_{j|i} \\ \sum_j r_{j|i} c_{j|i} & \sum_j r_{j|i}^2 c_{j|i}^2 & \sum_j r_{j|i}^2 s_{j|i} c_{j|i} \\ \sum_j r_{j|i} s_{j|i} & \sum_j r_{j|i}^2 s_{j|i} c_{j|i} & \sum_j r_{j|i}^2 s_{j|i}^2 \end{bmatrix}^{-1} \begin{bmatrix} \sum_j I_{j|i} \\ \sum_j r_{j|i} I_{j|i} c_{j|i} \\ \sum_j r_{j|i} I_{j|i} s_{j|i} \end{bmatrix}, \tag{3b}$$

and $s_{j|i} = \sin\delta_{j|i}$, $c_{j|i} = \cos\delta_{j|i}$. The coordinate x of $I_{j|i}$, A_i, p_i, q_i, and φ_i in Eq. (3) is omitted for simplicity.

In the second step, $r_{j|i}$ and $\delta_{j|i}$ are calculated with phase distribution $\varphi_i(x)$ as a known. To make LSQ-IA converge rapidly and accurately, $B_i(x) = \sqrt{p_i^2(x) + q_i^2(x)}$ is abandoned here [13–15]. We assume that for all the pixels in the fringe area D_i, the modulation is uniform, i.e. $B_i(x) = 1$ [13–15]. For the jth interferogram within the group, the phase shift and modulation variation factor are

$$\delta_{j|i} = \arctan\left(-\frac{q'_{j|i}}{p'_{j|i}}\right) \tag{4a}$$

and

$$r_{j|i} = \sqrt{p'^2_{j|i} + q'^2_{j|i}}, \tag{4b}$$

where

$$\begin{bmatrix} A_{j|i} \\ p'_{j|i} \\ q'_{j|i} \end{bmatrix} = \begin{bmatrix} N_i & \sum_x c'_i & \sum_x s'_i \\ \sum_x c'_i & \sum_x c'^2_i & \sum_x s'_i c'_i \\ \sum_x s'_i & \sum_x s'_i c'_i & \sum_x s'^2_i \end{bmatrix}^{-1} \begin{bmatrix} \sum_x I_{j|i} \\ \sum_x I_{j|i} c'_i \\ \sum_x I_{j|i} s'_i \end{bmatrix}, \tag{4c}$$
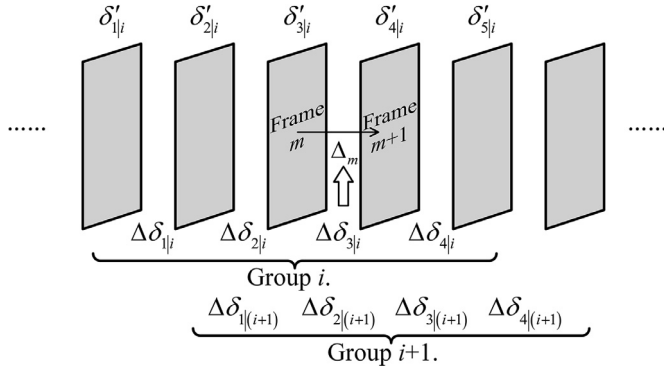
Fig. 2. Schematic diagram of step calculation, taking $N = 5$ as an example.

Fig. 3. The measured surface (a) and one of the generated interferograms (b) in the simulations.

and $s'_i = \sin\varphi_i$ and $c'_i = \cos\varphi_i$. In Eq. (4), the coordinate x of $I_{j|i}$, s'_i, c'_i, and φ_i is omitted. N_i denotes the number of pixels in D_i and summation signs are over the pixels in D_i as well. Here, background A is calculated as a frame-dependent parameter, but it is not transferred to the next cycle [15]. In each interferogram, at least one fringe is needed to ensure the matrix of Eq. (4c) nonsingular. Usually, ten iterations are enough to obtain a stable convergence result.

Step 2.3: Adjust the output values of phase shifts

The phase shifts obtained by LSQ-IA are wrapped in 0 to 2π. The output values of the phase shifts $\delta_{j|i}$ are unwrapped, and we get $\delta'_{j|i}$. Then, phase increments, i.e., $\Delta\delta_{1|i}$, $\Delta\delta_{2|i}$, ..., $\Delta\delta_{(N-1)|i}$, between frames of the ith group of interferograms are calculated by subtracting the phase shifts between adjacent frames, as shown in Fig. 2. Hence, we get the phase increments between consecutive frames in all groups. Finally, to reduce error, the phase increments calculated repeatedly between the mth frame and the $(m + 1)$th frame are averaged to obtain Δ_m, as the phase increment between the two frames. Thus, the scanning step between frame m and frame $(m + 1)$ is

$$z'_m = \frac{\lambda_0}{4\pi}\Delta_m. \tag{5}$$

The number of interferograms N in each group is 5 in this study, and there are four overlapped interferograms between two adjacent groups. The preset phase increment of the scanner is $\pi/2$. Thus in LSQ-IA, the initial input values of phase shifts are $\delta_{j|i} = (j-1)\pi/2$. The choice for number N and the overlap number is optimized, which can satisfy the assumption of Eq. (2) and make the initial values cover a period of 2π to average the influence of initial value setting.

Step 3: Reconstruct surface based on non-equal scanning steps

To obtain the surface height, the coherence envelope needs to be calculated from the non-equal scanning data. Traditional envelope sensing algorithms, such as the Hilbert transform method [16–18], Fourier transform method [19], and spatial frequency domain analysis [20], are only appropriate to the case of equal-step scanning and are not applicable here. The surface is reconstructed as follows.

Step 3.1: Calculate modulation and phase with least-squares method

Accumulating scanning steps between frames obtained in Eq. (5), we can determine the vertical position of each frame:

$$z_m = \begin{cases} 0, m = 1; \\ \sum_{i=1}^{m-1} z'_i, m \geq 2. \end{cases} \tag{6}$$

To facilitate the phase calculation, consecutive $(2L + 1)$ frames of interferograms are selected for each group, and L is a positive integer. For each pixel x in the interferogram, assuming the background and modulation remain constant in the group, its intensity within the ith group can be expressed as

$$I_{i+j} = A'_i + B'_i \cos\left[\phi_i + \frac{4\pi}{\lambda_0}\left(z_{i+j} - z_i\right)\right], j \in [-L, L], j \in (\mathbb{Z}), \tag{7}$$

where A'_i and B'_i are the background and modulation of pixel x in the ith group, and ϕ_i is the phase value of pixel x in the ith frame. The co-
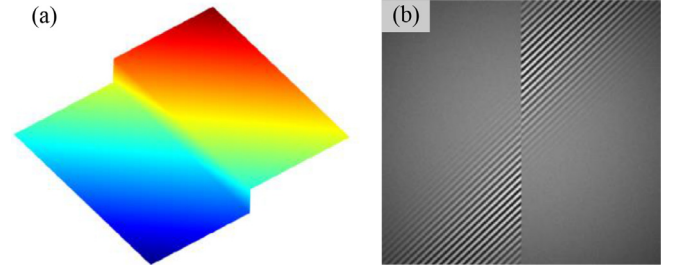
ordinate x of I_{i+j}, A'_i, B'_i, and ϕ_i is omitted. For the pixel x in the ith group, $A'_i(x)$ corresponds to $a(x)$, $B'_i(x)$ corresponds to $b(x)\exp[-(2\pi(z_i-h(x))/l_c)^2]$, and $\phi_i(x) = 4\pi[z_i-h(x)]/\lambda_0+\varphi_0$. Similar to Eq. (3), the modulation $B'_i(x)$ of pixel x in the ith group and the phase $\phi_i(x)$ in the ith frame can be calculated with least-squares method. Since the modulation of pixel x in the ith frame is repeated $(2L + 1)$ times in the traversal of each group, the average value as the modulation $M_i(x)$ of the ith frame is obtained, i.e., $M_i(x) =\sum_{-L}^{L}B'_{i+j}(x)/(2L+1)$. Here, using the accurately extracted scanning positions z, the modulations and phases of all the pixels in the interferograms are calculated. And $M(x)$ is also regarded as the envelope of WLI signal at pixel x.

Step 3.2: Fit the Gaussian envelope curve of modulation

Because the interference intensity is sensitive to noise, the distorted signal will lead to an incorrect calculation of the maximum modulation and result in a positioning error of zero fringe order [21]. Therefore, after obtaining the modulation of pixel x in each frame, a Gaussian curve fitting is performed to locate the envelope peak. And in addition, the polynomial fitting or gravity method can also be used for peak sensing.

Step 3.3: Determine the frame number of the closest point to the envelope peak

After the envelope peak is located, the closest sampling point to the envelope peak can be determined for each pixel. Then, with the phase value of pixel x, the surface height of x can be obtained as

$$h(x) = z_{n(x)}(x) - \frac{\lambda_0}{4\pi}\phi_{n(x)}(x). \tag{8}$$

Here $n(x)$ is the frame number of the closest point to the envelope peak.

In this section, we use the iterative algorithm to detect the scanning error. Different from Schmit's algorithm, which is based on the equal-step scanning of six adjacent frames and is only effective when coping with low-frequency disturbance or linear error, the proposed algorithm could compensate for random error accurately without approximation. Continuously moving fringes can satisfy the algorithm, which can also work for objects with varying slopes. And because the actual scanning steps are detected from collected interferograms, and the error is compensated for in surface reconstruction, the proposed algorithm is expected to achieve a high accuracy.
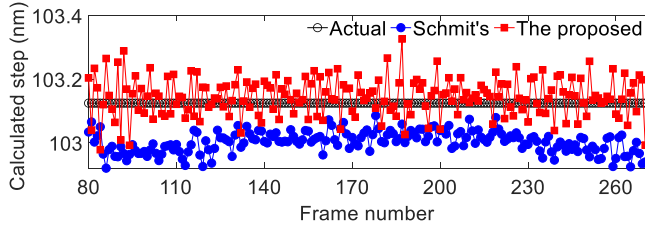
3. Simulations

To investigate the capability of the proposed algorithm, WLI with various types of scanning errors is simulated with a computer.

The equivalent wavelength of the light source with a Gaussian spectrum is $\lambda_0 = 550$ nm, and the spectral width is 100 nm. The preset scanning step is $\lambda_0/8 = 68.75$ nm. A step of 5 μm height is measured, as shown in Fig. 3(a). And a small amount of tilt is added to the step to ensure the fringes continuously moving during scanning. According to Eq. (1), the interferograms are generated. To simulate CCD sensor noises, normally distributed random noise with the standard deviation of 1% of the maximum intensity value (255 here) is added to the interferogram grayscale. And one of the generated interferograms is exhibited

Table 1
Linear errors in simulation.

Serial number	Linear error	Actual scanning step (nm)
1-1	0	68.75
1-2	25%	85.94
1-3	- 25%	51.56
1-4	50%	103.13
1-5	- 50%	34.38
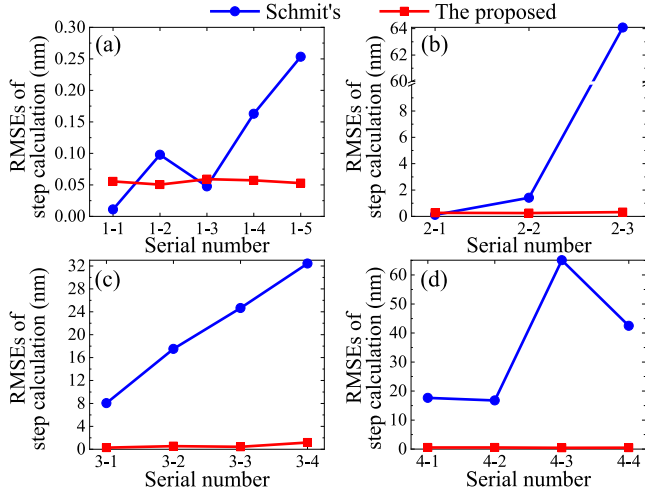
Fig. 4. RMSEs of scanning step calculation with two algorithms with different scanning errors: (a) linear error, (b) harmonic disturbance, (c) random noise, and (d) mixed disturbance.

Fig. 5. Comparison of the calculated scanning step of two algorithms with 50% linear scanning error.

in Fig. 3(b). Here, three types of scanning errors, linear error, harmonic vibration, and random noise, were simulated individually, and finally mixtures of the three errors were simulated. We use the accuracy of the calculated scanning step and reconstructed surface to evaluate the performance of the algorithm.

3.1. Accuracy of scanning step calculation

(1) Linear error

   Linear error is the most common type of errors of the piezoelectric scanners. In the simulation, five sets of interferograms are generated with scanning steps of 0, ± 25%, and ± 50% deviations from the preset value. The actual scanning steps of these five groups are shown in Table 1. The scanning steps are extracted from the interferograms with the proposed algorithm. The root mean squared errors (RMSEs) are used to evaluate the scanning step calculation accuracy, as shown in Fig. 4(a). Meanwhile, the scanning steps are also extracted with Schmit's algorithm as a comparison. Taking the 103.13 nm scanning step as an example, the calculated scanning steps with two algorithms are shown in Fig. 5. Although Schmit's algorithm is designed for linear scanning error compensation, the significant deviation from the nominal phase incre-

Table 2
Harmonic disturbances in simulation.

Serial number	Frequency	Amplitude (nm)
2-1	0.005	1000
2-2	0.04	150
2-3	0.3	50
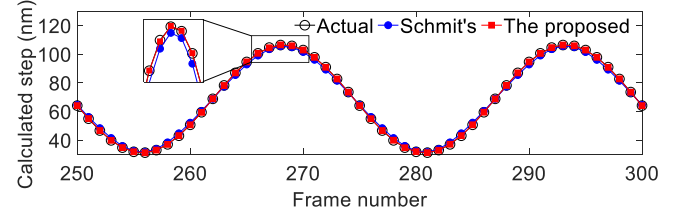
Fig. 6. Comparison of the calculated scanning step of two algorithms under harmonic disturbance 2-2.

Table 3
Random noises in simulation.

Serial number	Amplitude (nm)
3-1	20
3-2	40
3-3	60
3-4	80

ment value, $\pi/2$, leads to an obvious calculation error. In contrast, scanning steps calculated with the proposed algorithm converge to the actual value. The calculation accuracy of the proposed algorithm is higher overall and is not easily affected by the linear error.

(2) Harmonic disturbance

   Harmonic vibration is one of the most fundamental forms of vibration in the environment. To test the capability of the proposed algorithm, harmonic disturbances of three different frequencies and amplitudes are added in the scanning steps, as shown in Table 2. Here, the vibration frequency is normalized to the interferogram acquisition frequency. Fig. 4(b) shows the RMSEs of scanning step calculation with two algorithms. And a comparison of the calculated scanning step with two algorithms is shown in Fig. 6. Limited by the principle, although Schmit's algorithm is accurate in the presence of low-frequency vibration, it has significant errors under higher frequency disturbance. Nevertheless, the proposed algorithm could detect scanning error accurately in vibration disturbance over a wide frequency band.

(3) Random noise

   The positioning error of the scanner and environmental vibration produce random noises in scanning steps. Uniformly distributed random noises with four different amplitudes in Table 3 are added to the preset step when generating interferograms. As shown in Fig. 4(c), in this case the proposed algorithm has nearly constant detection accuracy when random noise increases.

(4) Mixed disturbance

   There are usually many types of vibration in the practical environmental disturbance, such as in the machining workshop. Hence, a mixture of the above three types of disturbances is added to the scanning steps, of which the parameters are shown in Table 4. The scanning step calculation errors are shown in Fig. 4(d). As an example, Fig. 7 shows the calculated scanning steps with disturbance 4-4. This simulation indicates that the proposed algorithm could cope with fast-changing and complex disturbances.

   From the results of simulations, it can be seen that all of the RMSEs of scanning steps calculated with the proposed algorithm are less than

Table 4
Mixed disturbances in simulation.

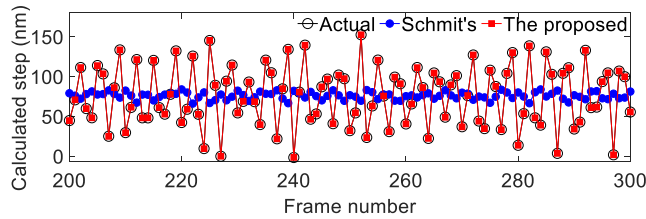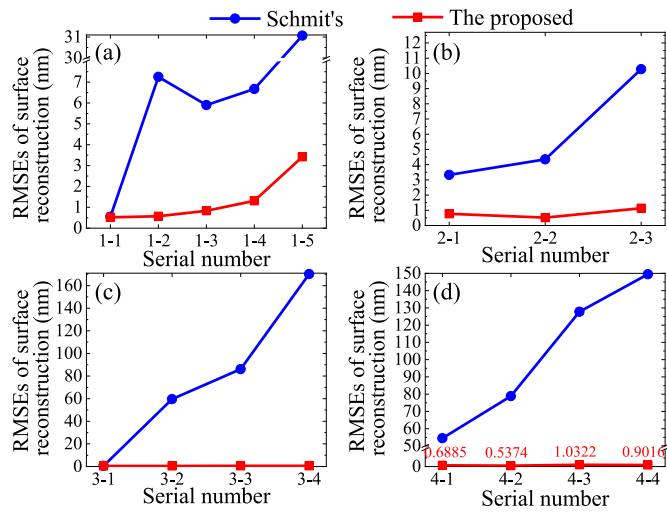| Serial number	Linear error	Harmonic disturbance		Random noise
		Frequency	Amplitude (nm)	Amplitude (nm)
4-1	0	0.005	1000	40
4-2	0	0.04	150	40
4-3	0	0.3	50	40
4-4	10%	0.3	30	40

Fig. 7. Comparison of the calculated scanning step of two algorithms under mixed disturbance 4-4.

Fig. 8. RMSEs of surface reconstruction with two algorithms with different scanning errors: (a) linear error, (b) harmonic disturbance, (c) random noise, and (d) mixed disturbance.

1.2 nm, and the algorithm shows significant superiority under a higher frequency vibration.

3.2. Accuracy of surface reconstruction

The surface reconstruction accuracy is evaluated with the calculated scanning steps. The pixel-to-pixel deviation of the reconstructed surface height from the true surface, called residual error, is calculated, and the RMS value of residual errors is used to evaluate the reconstruction accuracy. Fig. 8 shows the surface reconstruction errors under the influence of different scanning errors. Fig. 9 compares the residual error distributions under the mixed disturbance 4-4. Owing to the accurate scanning step calculation and compensation, the ripples caused by vibration are significantly attenuated with the proposed algorithm.

Next, the step height accuracy of the reconstructed surface is investigated. The absolute error of step height reconstructed by the proposed algorithm is less than 3 nm. In contrast, that by Schmit's algorithm reaches a maximum of 36 nm.

The above simulations verify that the proposed algorithm has advantages of a high accuracy and strong immunity to various types of scanning errors, and shows good resistance to wideband vibration.
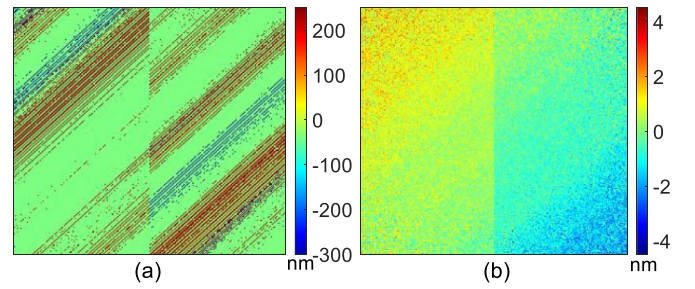

Fig. 9. The residual errors of the reconstructed step surfaces under mixed disturbance 4-4: (a) by using Schmit's algorithm, and (b) by using the proposed algorithm.
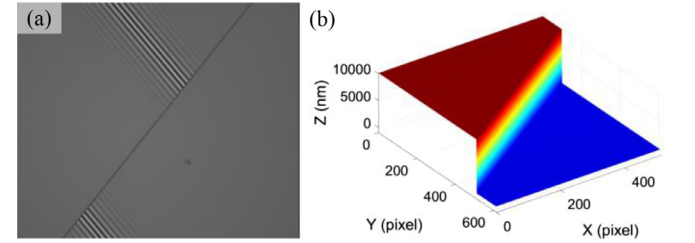

Fig. 10. One interferogram (a) and the reconstructed surface of the 10 μm step (b).

4. Experimental verification

A step height standard and a flat are measured to verify the measurement accuracy and vibration resistance of the proposed algorithm. The used white-light interferometer is configured with a 10× Mirau-type interference objective with numerical aperture 0.3, and the measurement area is 1.70 mm × 1.42 mm. The light source is a white LED with a Gaussian spectrum, and works in the continuous mode. The coherence length of the light source is 4 μm. The CCD camera resolution is 616 × 514 pixels, the interferogram acquisition frequency is $f_0 = 50$ Hz, and the integration time is 15 ms. Scanning is realized by a motor with screw. The scanning step is set to be 68.75 nm. The interferometer is mounted on an optical platform without vibration isolations. The measured workpiece is fixed on a pre-loaded translational stage. A PZT is used to push the stage to generate the required vibrations, and an interferometric displacement sensor is used to monitor the real-time vibrations of the stage. The equivalent wavelength of the interferometer was calibrated with a step height standard of nominal height 1.8 μm (measurement value 1.768 ± 0.010 μm) before measurement. The step height standard was measured 8 times in the static environment, and the equivalent wavelength is $\lambda_0 = 595.9$ nm.

4.1. Step height standard measurement

A step height standard of nominal height 10 μm (measurement value 10.012 ± 0.022 μm) was measured to test the measurement accuracy of the proposed algorithm. The step was tilted by about 10 mrad to ensure that the fringes move continuously across the measurement area during scanning. First, the step was measured 8 times in the static environment. One of the interferograms and the reconstructed surface of the step are shown in Fig. 10. The measured mean height values with Schmit's algorithm and the proposed algorithm are 9.9637 μm and 9.9998 μm respectively. And the step height value is evaluated according to ISO 5436-1. The standard deviations of step height of 8 measurements are used to estimate the repeatability, which are 1.10 nm and 0.99 nm, respectively.

Then, the step height standard was measured under harmonic vibration disturbances. The PZT produced harmonic vibrations with amplitudes of 20, 30, and 40 nm and frequencies ranging from 5 Hz to
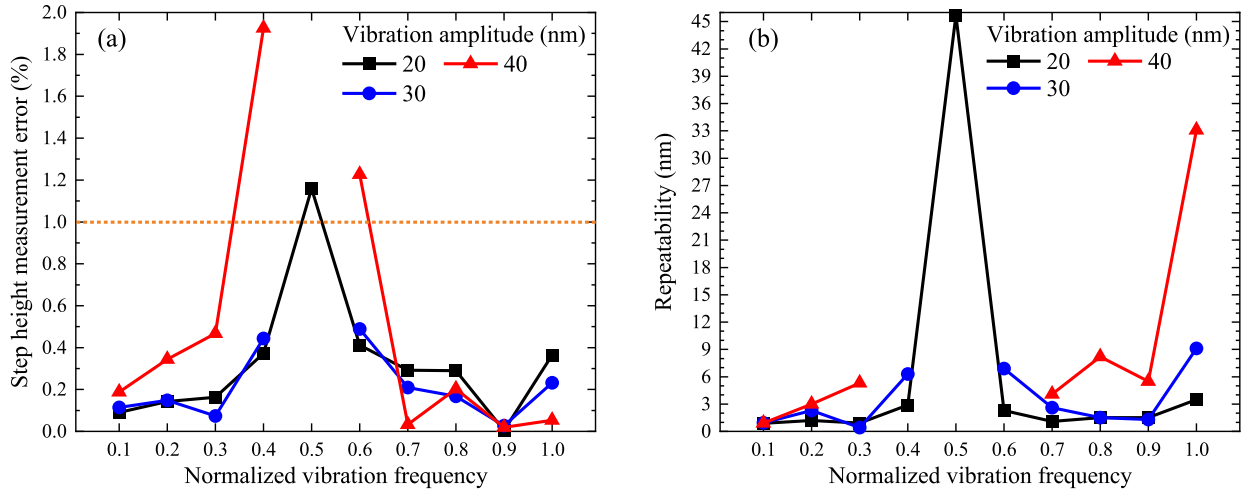
Fig. 11. The step height measurement error (a) and repeatability (b) with Schmit's algorithm.
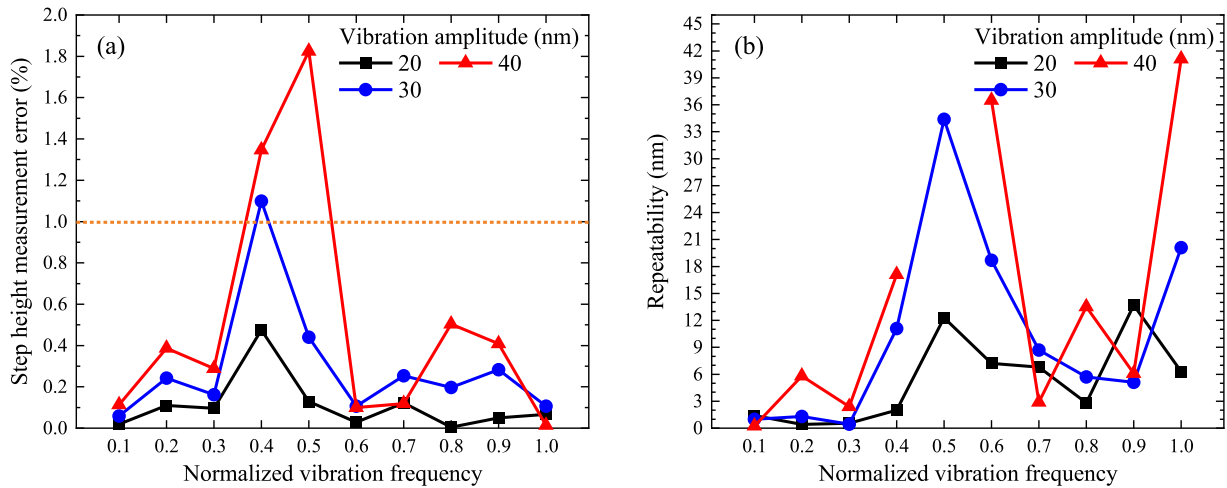

Fig. 12. The step height measurement error (a) and repeatability (b) with the proposed algorithm.

50 Hz (with 5 Hz interval). The step height standard was measured 8 times under each harmonic vibration. The measurement errors of step height with respect to vibration are shown in Figs. 11 and 12, where the vibration frequency f is normalized to the interferogram acquisition frequency f_0. The dropped data points in the plots mean that the values are significantly out of the ordinate range. Overall, the step height errors with the proposed algorithm are smaller than those with Schmit's algorithm. With the proposed algorithm, the relative errors of step height are less than 2% over the whole vibration frequency. And the repeatability of measurements is mostly better than 20 nm, as shown in Fig. 12(b), which is tolerable. Nevertheless, Schmit's algorithm shows a better repeatability, owing to its averaging effect. The results show that the proposed algorithm has acceptable vibration resistance over a wide frequency band.

Besides, an experiment of measuring a step of 89 nm-height also shows that the proposed algorithm has almost the same relative accuracy when measuring very shallow structures.

4.2. Chrome-coated mirror measurement

For WLI working under vibration, another concerned aspect is the suppression of ripple error that lowers the accuracy of surface measurement [11]. Therefore, the performance of the proposed algorithm was further investigated by measuring the surface roughness of a chrome-coated mirror, which was tilted by 6 mrad in experiment. The param-

eter Sq, is used to evaluate the surface roughness. First, the mirror in the static environment was measured 8 times, the mean value of surface roughnesses by using Schmit's algorithm and the proposed algorithm are 2.2538 nm and 1.9262 nm, and the repeatability of measurements are 0.1364 nm and 0.0742 nm. In roughness calculation, the surface is leveled.

Then, the mirror was measured under the same harmonic disturbances as those in Sec. 4.1. Figs. 13 and 14 show the measurement values and repeatability of measured surface roughness by using Schmit's algorithm and the proposed algorithm. Compared with the measured roughnesses without vibration, the maximum deviation of Schmit's algorithm is up to 9.43 nm, while that of the proposed algorithm is 1.52 nm. Taking the surface measured under the harmonic disturbance of frequency $0.2 f_0$ and amplitude 40 nm as an example, the leveled surface maps are shown in Fig. 15. The proposed algorithm has significant improvement in ripple error suppression.

5. Discussions

5.1. Limitation of step error calculation

In *Step 2.3* of the proposed algorithm, the unwrapping will fail if the step error is large, and consequently the vibration resistance is limited. Hence it is necessary to analyse the limitation in detail. Supposing the preset value of the phase increment between two adjacent frames is Δ_0
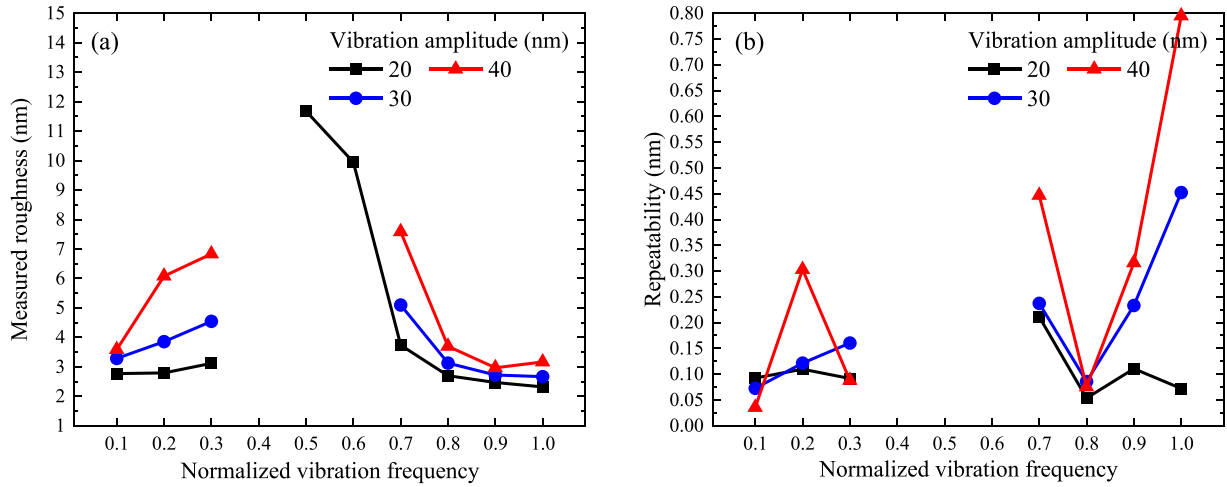
Fig. 13. The measurement values (a) and repeatability (b) of measured surface roughness with Schmit's algorithm.
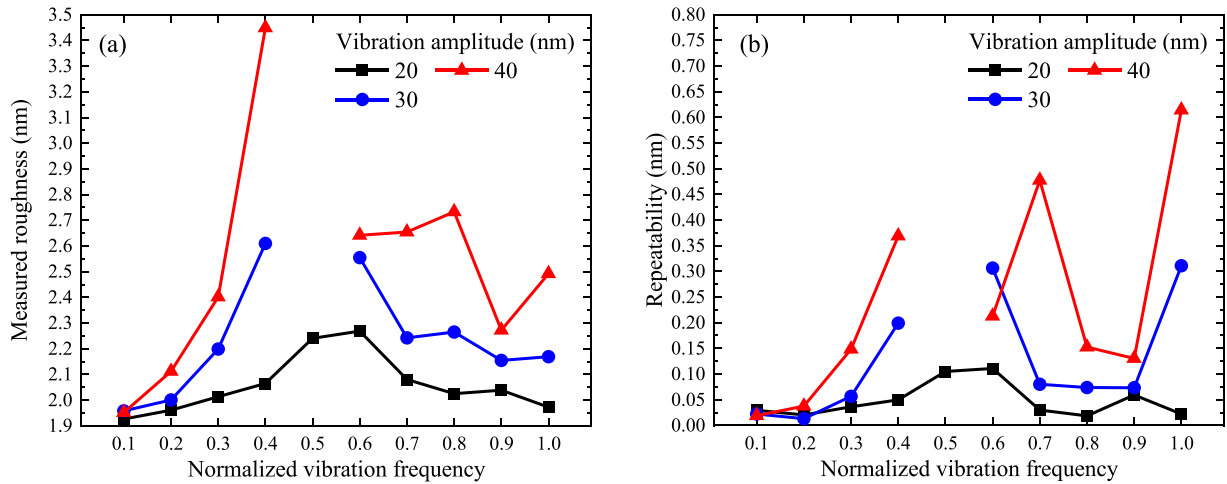

Fig. 14. The measurement values (a) and repeatability (b) of measured surface roughness with the proposed algorithm.
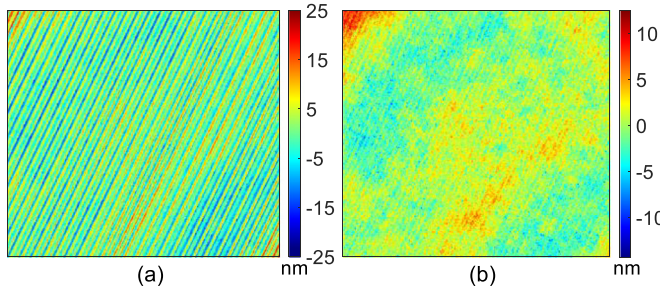

Fig. 15. The leveled surface maps measured under the harmonic disturbance of frequency $0.2 f_0$ and amplitude 40 nm: (a) by using Schmit's algorithm, and (b) by using the proposed algorithm.

and the maximum phase increment deviation is Δ_ε, the actual phase increments Δ' between adjacent frames are between $\Delta_0 - \Delta_\varepsilon$ and $\Delta_0 + \Delta_\varepsilon$. It can be concluded that:

a) When $\Delta_0 + \Delta_\varepsilon \leqslant \pi$, phase increments are not wrapped.

b) When $\Delta_0 + \Delta_\varepsilon > \pi$, and $\Delta_0 + \Delta_\varepsilon - 2\pi < \Delta_0 - \Delta_\varepsilon$, i.e., when $\pi - \Delta_0 < \Delta_\varepsilon < \pi$, the phase increments over π are wrapped, and their wrapped values $\Delta' - 2\pi$ are lower than the minimum of the actual phase increments, which is $\Delta_0 - \Delta_\varepsilon$. Therefore, the phase increments below $\Delta_0 - \Delta_\varepsilon$ can be corrected by adding 2π. Meanwhile, under the

condition of $\Delta_\varepsilon < \pi$, $\Delta_0 + \Delta_\varepsilon - 2\pi < \Delta_0 - \pi < \Delta_0 - \Delta_\varepsilon$ is established, and $\Delta_0 - \pi$ is between the wrapped value and the lower boundary of the actual phase increments. Hence, correction can be achieved by adding 2π to the part below $\Delta_0 - \pi$. It is not necessary to know the exact amplitude of phase increment deviation Δ_ε.

c) When $\Delta_0 + \Delta_\varepsilon > \pi$, and $\Delta_0 + \Delta_\varepsilon - 2\pi \geqslant \Delta_0 - \Delta_\varepsilon$, i.e., when $\Delta_\varepsilon \geqslant \pi$, the phase increments over π are wrapped. The wrapped value is mixed with some actual phase increments and cannot be distinguished. In this case, the phase increment cannot be unwrapped correctly.

Thereby, the maximum deviation of phase increments that the proposed algorithm can accept is π, corresponding to the scanning step error $\lambda_0/4$. However, as the scanning step deviation increases, LSQ-IA may converge to a value with the opposite sign, determined by the initial value of iteration. This further leads to limitation of step error calculation. In simulations and experiments, when the deviation of scanning step exceeds 80 nm, i.e. $0.13 \lambda_0$, the reverse converge appears, which results in step calculation error and surface reconstruction failure. Thus, the proposed algorithm is able to detect and compensate for scanning step error within $0.13 \lambda_0$ in reality.

5.2. Impact of harmonic vibration

It is supposed that the harmonic vibration amplitude is A and the frequency is f, and the interferogram acquisition period is $T_0 = 1/f_0$. Disturbed by the harmonic vibration, the maximum scanning step error

is

$$A_m = 2 \cdot A \sin\left(2\pi f \cdot \frac{T_0}{2}\right) = 2A \sin\left(\frac{\pi f}{f_0}\right). \tag{9}$$

When $f = f_0/2$, the scanning step deviates from the preset value maximumly, and the deviation is twice the amplitude A of the harmonic vibration. In this case, the step extraction error also increases, leading to a more significant error on the measured surface, which can be seen in experiments. With a normalized vibration frequency of 0.5, the method proposed in this paper still achieves relatively accurate measurements. The relative errors of step height are less than 1.4%, as long as the scanning step error is not limited by phase unwrapping.

In addition, the harmonic disturbance causes variation in fringe contrast. Higher frequency vibration has a more profound influence on the fringe quality, which impacts scanning step calculation. The contrast variation can be reduced by shortening the camera integration time in practice.

6. Conclusions

In this paper, we propose an effective algorithm for detecting and compensating for scanning error for WLI. The algorithm calculates scanning steps without approximation, and shows a good reconstruction accuracy when WLI is disturbed by linear error, harmonic disturbance, random noise, and mixed disturbance. Practical measurements demonstrate that the accuracy of 10 μm step height standard measurement is better than 1.4% under the harmonic vibration. Meanwhile, the ripple error is significantly suppressed, and the roughness measurement error is less than 2 nm. The proposed algorithm relaxes the environment requirement of white-light interferometer application. It can be applied to white-light interferometers used in a noisy environment, such as in an ultra-precision machining workshop.

Declaration of Competing Interest

The authors declare that they have no known competing financial interests or personal relationships that could have appeared to influence the work reported in this paper.

CRediT authorship contribution statement

Kaihua Cui: Methodology, Software, Data curation, Writing – original draft. **Qian Liu:** Conceptualization, Methodology, Writing – review & editing, Supervision. **Xiaojin Huang:** Validation. **Hui Zhang:** Resources. **Lulu Li:** Resources, Supervision.

References

[1] Hu C, Liu X, Yang W, Lu W, Yu N, Chang S. Improved zero-order fringe positioning algorithms in white light interference based atomic force microscopy. Opt Laser Eng 2018;100:71–6.
[2] Pavliček P, Mikeska E. White-light interferometer without mechanical scanning. Opt Laser Eng 2020;124:105800.
[3] Ma L, Jia J, Pei X, Sun F, Zhou H, Li J. A robust surface recover algorithm based on random phase noise correction for white light interferometry. Opt Laser Eng 2020;128:106016.
[4] Conroy M, Armstrong J. A comparison of surface metrology techniques. J Phys: Conf Ser 2005;13(1):458–65.
[5] Caber PJ. Interferometric profiler for rough surfaces. Appl Opt 1993;32(19):3438–41.
[6] Cohen DK, Caber PJ, Brophy CP. Rough surface profiler and method. U.S. patent 5133601;1992 Jul.(28).
[7] Shen MH, Hwang CH, Wang WC. Using higher steps phase-shifting algorithms and linear least-squares fitting in white-light scanning interferometry. Opt Laser Eng 2015;66:165–73.
[8] Chen LC, Yeh SL, Tapilouw AM, Lee KF. In-situ scanning white light interferometry employing dual-sensing configuration and active fringe-locking strategy. Int J Nanomanuf 2012;8(1/2):40–53.
[9] Gao F. Interferometry for online/in-process surface inspection. London, UK: InTech; 2017. p. 41–59.
[10] Tereschenko S, Lehmann P, Zellmer L. Brueckner-Foit A. Passive vibration compensation in scanning white-light interferometry. Appl Opt 2016;55(23):6172–82.
[11] Schmit J, Olszak A. High-precision shape measurement by white-light interferometry with real-time scanner error correction. Appl Opt 2002;41(28):5943–50.
[12] Okada K, Sato A, Tsujiuchi J. Simultaneous calculation of phase distribution and scanning phase shift in phase shifting interferometry. Opt Commun 1991;84(3-4):118–24.
[13] Wang Z, Han B. Advanced iterative algorithm for phase extraction of randomly phase-shifted interferograms. Opt Lett 2004;29(14):1671–3.
[14] Liu Q, Wang Y, He J, Ji F. Phase shift extraction and wavefront retrieval from interferograms with background and contrast fluctuations. J Opt 2015;17(2):025704.
[15] Liu Q, Zhang H, Huang X, Cui K, Li L, Yue X. Vibration-resistant interference microscope with assistant focusing for on-machine measurement of surface topography. Precis Eng 2020;66:220–8.
[16] Pavliček P, Michálek V. White-light interferometry—Envelope detection by Hilbert transform and influence of noise. Opt Laser Eng 2012;50:1063–8.
[17] Pavliček P, Mikeska E. Fast white-light interferometry with Hilbert transform evaluation. Proc SPIE 2016;10142:101420Y.
[18] Li Y, Kästner M, Reithmeier E. Vibration-insensitive low coherence interferometer (LCI) for the measurement of technical surfaces. Meas 2017;104:36–42.
[19] Chim SS, Kino GS. Phase measurements using the Mirau correlation microscope. Appl Opt 1991;30(16):2197–201.
[20] Groot PD, Deck L. Surface profiling by analysis of white-light interferograms in the spatial frequency domain. J Mod Opt 1995;42(2):389–401.
[21] Vo Q, Fang F, Zhang X, Gao H. Surface recovery algorithm in white light interferometry based on combined white light phase shifting and fast Fourier transform algorithms. Appl Opt 2017;56(29):8174–85.